MODELING STUDIES ON THE PRECIPITATION OF Kr AFTER IMPLANTATION INTO METALS*

J. Rest
Materials and Components and Technology Division

R. C. Birtcher and A. S. Liu
Materials Science Division
Argonne National Laboratory
Argonne, IL 60439

February 1988

DISCLAIMER

To be presented at the 14th International Symposium on Effects of Radiation on Materials, June 27-29, 1988, Andover, MA.
*Work supported by the U. S. Department of Energy, BES-Materials Sciences, under Contract W-31-109-Eng-38.

MODELING STUDIES ON THE PRECIPITATION OF Kr AFTER IMPLANTATION INTO METALS*

J. Rest
Materials and Components and Technology Division

R. C. Birtcher and A. S. Liu
Materials Science Division
Argonne National Laboratory
Argonne, IL 60439

Abstract

A rate-theory approach is applied to interpreting observations on the precipitation of Kr injected into Ni at temperatures between 25 and 560°C. At temperatures of 400°C or higher, the implanted Kr precipitates evolve into a bi-modal size distribution containing small solid precipitates and an additional population of larger, faceted bubbles. The calculations explore the dependence of the observed bi-modal distribution on the maximum size of the solid Kr precipitates and the effect of this dependence on bubble mobility. The analysis suggests that during the irradiation whereas the large bubbles move by surface diffusion, the solid Kr precipitates are immobile. The relevance of the Kr-Ni interaction on the solid Kr precipitates size cutoff is discussed.

*Work supported by the U. S. Department of Energy, BES-Materials Sciences, under Contract W-31-109-Eng-38.

MODELING STUDIES ON THE PRECIPITATION OF Kr AFTER IMPLANTATION INTO METALS*

J. Rest
Materials and Components and Technology Division

R. C. Birtcher and A. S. Liu
Materials Science Division
Argonne National Laboratory
Argonne, IL 60439

1. Introduction

Recent studies on the precipitation of Kr injected into Ni at temperatures between 25 and 560°C [1] have revealed that at temperatures of 400°C or higher the implanted Kr forms a bi-modal size distribution containing small solid precipitates and an additional population of larger, faceted bubbles. The small Kr precipitates are fcc crystals whose lattices are aligned with the Ni lattice: the Kr is held in the solid state by the interatomic forces between the Kr-Kr and the Kr-Ni atoms (the mismatch between the Kr and Ni lattice constants is as large as 55%). As the Kr cavity size increases, the average spacing between the Kr atoms increases, decreasing the magnitude of the Kr-Kr interaction. The average Kr lattice parameter, determined from electron diffraction at room temperature, increases with increasing Kr fluence from 0.515 nm to an asymptotic value of about 0.545 nm. This increase towards an asymptotic limit is due to expansion of the Kr lattice as precipitates grow, until the decrease in cavity pressure allows melting of solid Kr in the relatively large cavities.

Previous analytical studies have attributed the observed bi-modal distribution of He gas bubbles formed in irradiated metals at relatively high temperature ($> 0.4\ T_m$) to bubble coalescence [2] or to the existence of a

*Work supported by the U. S. Department of Energy, BES-Materials Sciences, under Contract W-31-109-Eng-38.

critical radius for bubble stability [3]. The key assumption used is that the continuously generated inert gas atoms are primarily involved in small bubble nucleation and growth: this give rise to a peak at small bubble sizes in size distribution. The peak at larger sizes is caused by bubble coalescence. The over all shape of the bubble size distribution is controlled by the interaction between these two bubble populations. The detailed behavior was found to depend strongly on the mechanism of bubble migration (e.g., surface diffusion vs volume diffusion).

However, bubble coalescence alone is insufficient to explain the current experiments where the observed bimodal distribution occurs at much lower temperatures ($\leq 0.39\ T_m$), and where the small precipitates are solid Kr. Recent theories [4,5] on bubble diffusion in ionic materials have considered the basic transport mechanism to be non-localized surface diffusion limited by the interaction between the diffusing surface defect and the gas in the bubble. An extension of these ideas to the case of solid Kr precipitates yields a drastic reduction of the bubble mobility by surface diffusion in the presence of a very high pressure gas [6] due to the strength of the interaction between the diffusing atom and the "close-packed" Kr atoms.

In order to gain insight into the relevant physical processes which dominate the behavior of Kr in metals at relatively low temperatures, the present paper examines theoretically the effect of solid gas on bubble mobility and bubble coalescence.

2. Experiment

Thin single-crystal Ni films (70 nm thick) were prepared by evaporation of high purity Ni in a vacuum less than $1 \cdot 10^{-7}$ Torr onto freshly cleaved NaCl at a temperature of 350°C. The coated NaCl was cleaved into small pieces, and

specimens were floated on a water-methanol mixture onto Cu TEM grids. Implantations were performed with 180 keV Kr^+ ions at fluxes less than $2 \cdot 10^{16}$ $m^{-2}sec^{-1}$. During implantation, the TEM grids were clamped at their periphery against a Cu disk, and the entire assemble was mounted on a plate that could be heated to the desired temperature. The implantation energy was selected on the basis of the results from the TRIM computer code [7]. At 180 keV, the Kr concentration depth profile within the Ni films peaks near the foil center and decreases to near zero at both foil surfaces. Estimates for a fluence of $1 \cdot 10^{20}$ m^{-2} yield a damage level of 33 displacements per atom at the location of the peak in the kr concentration of 3.14 atomic percent. Sputtering for this fluence will cause the depth peaks to shift nearer the back specimen surface by 110 Å (or less due to reduced sputtering of the surface oxide) [8]. This will make the Kr concentration more uniform.

Post implantation, TEM observations were made with a JEOL JEM-100-CX at an operating voltage of 100 keV and at magnifications up to 100,000 times. Details within the specimens greater than 1 nm were detectable. The gas-filled cavities were imaged in bright field by their defocus contrast. Selected-area diffraction patterns were produced with the electron beam parallel to the <100> specimen normal, and a traveling, optical microscope was used to determine the average solid-Kr lattice parameter from the positions on the micrograph of intensity maxima due to Kr and Ni {200} reflections. The estimated uncertainty was 0.5 percent due to weakness of the Kr reflections and the over exposure of the film by the Ni diffraction spots. The solid Kr precipitates were imaged in dark field from electrons scattered into a Kr {200} reflection. In situ elevated-temperature measurements were made with a heating stage, however specimen oxidation restricted the observations to temperatures of about 500°C.

Examples of TEM images and electron diffraction patterns from Ni implanted with Kr at 500°C are shown in Fig. 1. Electron diffraction patterns show both the spots due to the Ni lattice and additional adjacent spots due to solid Kr. The additional spots have the same symmetry as the spots from the Ni lattice, but arise from a lattice with a much larger lattice parameter. The extra diffraction is always in coincidence with that from the Ni lattice. Dark-field images made with the extra reflections show that they arise from solid, fcc Kr precipitates [1]. The existence of such diffraction spots indicates that the individual Kr crystallites are aligned with each other and the Ni lattice. The alignment of solid Kr with the Ni lattice occurs upon precipitation of the Kr regardless of the implantation temperature (the maximum temperature in this study was 560°C). Precipitates larger than about 30 Å radius are not solid, but are liquid or gas. The spherical precipitates are solid, while the larger faceted precipitates are not. At fluence below $1x10^{22}$ m^{-2}, the size distribution contains only small, spherical precipitates (radius less than 30 Å). However, as the fluence is increased, the size distribution becomes bi-modal and contains both small, spherical, and larger faceted precipitates.

The bubble size distribution for implanted Kr in Ni at 500-534°C as a function of the Kr^+ fluence is shown in Fig. 2. At low Kr^+ doses ($<1.0x10^{20}$ m^{-2}), the distribution is monomodal consisting of solid precipitates with the peak occurring at a radius of about 20 Å. As the Kr fluence increases, the peak of the distribution tends to shift to a larger precipitate radius and by $1 \cdot 10^{20}$ m^{-2} the tail of the distribution extends to larger sizes. As the Kr fluence is increased further, the monomodal distribution evolves into a bimodal distribution with the secondary peak occurring at about a 50 Å radius. As the fluence is increased from 2 to $4x10^{20}$ m^{-2}, the primary peak

(solid Kr precipitates) remains unchanged, while the number of bubbles in the secondary peak (gaseous or liquid Kr) increases. It should be noted that between 2 and 4×10^{20} m^{-2} the large Kr bubbles rupture to the specimen surface with a subsequent loss of gas from the sample. This effect limits further evaluation of the distributions shown in Fig. 2. Thus, as the Kr fluence is increased at 500-534°C, the distribution of the solid Kr precipitates remains basically static while the number of the larger bubbles increases.

3. Model

The calculations are based on a rate-theory approach as embodied in the GRASS-SST model [9,10]. GRASS-SST includes gas behavior mechanisms such as bubble nucleation, migration and coalescence. The calculation classifies the bubbles in terms of the number of gas atoms per bubble: the radius of each class depends upon the Kr equation of state and vacancy dynamics. A system of coupled nonlinear differential equations is used to calculate the evolution of bubbles between classes. This system of equations is solved incrementally as a function of time in order to obtain the evolution of the bubble densities. For each time increment, GRASS-SST solves equations having the form

$$\frac{dF_i}{dt} = - A_i F_i F_i - B_i F_i + C_i \quad (i = 1,\ldots,N), \qquad (1)$$

where F_i is the number of bubbles in the ith size class per unit volume, and the coefficients B_i and C_i are functions of all F_j's, $j \neq i$; A_i represents the rate at which bubbles are lost from (grow out of) the ith size class due to coalescence with bubbles in that class; B_i represents the rate at which bubbles are lost from the ith size class due to other processes, such as coalescence with bubbles in other size classes, and C_i represents the rate at

which bubbles are being added to the ith size class due to processes such as bubble coalescence.

The probability of, P_{ij}, of i and j bubbles coalescing is given by $P_{ij} = 4\pi (r_i + r_j) (D_i + D_j)$, where r_i is the bubble radius and D_i is the diffusion coefficient for the ith class. For the case of surface controlled bubble motion, the limiting step is defect jumps around the inside bubble surface: the bubble mobility D_i is given by [4]

$$D_i = \frac{3\Omega^{4/3}}{2\pi r_i^4} D_g W . \qquad (2)$$

where Ω is the molecular volume of the crystalline solid, D_g is the diffusion coefficient of the surface defect through the gas in the bubble, and W is the fraction of surface atoms which can participate in the diffusion process. Some authors have asserted that bubble migration and coalescence is only a significant growth mechanism over a small bubble size range, since when the bubbles grow larger they develop facets and the nucleation of ledges on these facets becomes the rate-controlling step for migration [11,12]. However, migration dominated by ledge nucleation requires the presence of atomically smooth facets, a condition not likely to be found during ion implantation where considerable damage is being sustained by the material. Thus, although step nucleation is a reasonable mechanism of bubble diffusion during isothermal anneals, this analysis assumes that surface diffusion control is the appropriate mechanism of gas-bubble mobility in an irradiation environment [13].

Bubble diffusion as described by eq. 2 assumes that the basic transport mechanism is surface diffusion limited by interaction between the diffusing surface defect and the gas in the bubble [4,5]. An extension of these ideas

to the case of solid Kr precipitates yields a drastic reduction of the surface mobility of adatoms in the presence of a very high pressure gas [6] due to the strength of the interaction between the diffusing adatom and the "close-packed" Kr atoms. For bubble size classes below the maximum solid Kr precipitate size (i.e., the solid-bubble cutoff, r_c), zero bubble mobility is assumed. Larger bubbles (at the cutoff and beyond) are assumed to move by surface diffusion with the mobility given by eq. 2. The diffusional growth of nonequilibrium intragranular bubbles is based on an analysis by Gruber [14]. The rate of change of the bubble radius is given by

$$\frac{dr_i}{dt} = \frac{D_u}{r_i} \left\{ 1 - \exp\left[- \left(P_i - P_h - \frac{2\gamma}{r_b} \right) \frac{\Omega}{kT} \right] \right\}, \tag{3}$$

where D_u is the vacancy diffusion coefficient; kT, the thermal energy; P_i, the internal gas pressure; P_h, the external hydrostatic pressure; and γ, the surface energy. In order to simplify the calculation, a relaxation time approximation is utilized of the form [15]:

$$r_i = r_i^o + (r_i^{eq} - r_i^o)(1 - e^{-t/\tau}), \tag{4}$$

where τ is defined by the initial growth rate calculated using eq. (3) and r_i^o is the radius of the ith class at the start of the time increment. The equilibrium radius for each class, r_i^{eq}, is obtained by using a Kr equation of state and the generalized capillary relation,

$$P_i = \frac{2\gamma}{r_i} - P_h. \tag{5}$$

The Kr equation of state is based on a perturbed hard-sphere model [16] using a Lennard-Jones 12-7 potential which has the form

$$\frac{\frac{4}{3}\pi r^3 P}{RT} = Z^{hs}(a) - dbf(T) - \Delta Z,$$

where (6)

$$Z^{hs} = \frac{1 + y - y^2 - y^3}{(1 - y)^3},$$

and $\gamma = bd/4$.

In eq. 6, d is the gas density, b is the effective volume of the gas, f(T) is a function which can be calculated for a given interatomic potential, and has the form

$$f(T) = \sum_{1}^{\infty} \beta^n q_n^n . \quad \text{With } \beta = 1/T \text{ and } q_n = \text{constants.} \tag{7}$$

The effective volume of the gas, b, is given by

$$b = \frac{2}{3} \pi A_v \sigma^3 [B^* + f(T)], \tag{8}$$

where

$$B^* = 3/\sigma^3 \int_0^{\infty} [1 - \exp(-u/kT)] r^2 dr \tag{9}$$

The interatomic potential used in evaluating eq. (9) is the Lennard-Jones (12,7) potential

$$u(R) = \varepsilon F(12,7) [(\sigma/r)^{12} - (\sigma/r)^7], \tag{10}$$

where F(12,7) is a constant. The ΔZ term in eq. (6) is essentially a correction term which is proportional to the gas density to powers higher than 1 and is determined by a fit to experimental data.

4. Results of Calculations

In this section, the effects of fluence on the precipitate-size distribution are discussed. In order to first set the stage for these calculations, bubble distributions are first calculated for different values of the solid-bubble cutoff, r_c, and the gas-bubble diffusivity, D_i. Values for these parameters are shown in Table 1.

Table 1.
Values for Various Parameters used in GRASS-SST Calculations of the Kr Bubble Distribution in Ni

r_c	22 Å
D_i	D_o/r_i^4
D_o	$1.6 \cdot 10^{-46}$ (m^2/sec)
γ	2 J/m^2

Figure 3 shows the results of GRASS-SST calculations of the Kr bubble-size distribution in Ni at 500°C and at a fluence of 2×10^{20} m^{-2} for three values of the solid-gas bubble cutoff (11, 12, and 31 Å). As shown in Fig. 3, decreasing the cutoff shifts the small bubble peak to smaller bubble sizes while at the same time broadening the distribution of the large bubbles.

The small-bubble peak extends up to the largest size class which contain solid Kr bubbles. This peak occurs because the larger solid bubbles provide a greater cross-section for single gas atom capture than smaller precipitates, and because the immobile solid bubbles do not participate in bubble-bubble coalescence processes, but grow only by the trapping of single gas atoms.

The peak in the distribution at larger bubble sizes occurs because of bubble-bubble coalescence processes. This is clearly seen in Fig. 4 where GRASS-SST calculations of the bubble-size distribution for three values of the bubble diffusivity, D_i, are presented. The bi-modal distribution narrows for reduced values of bubble diffusivity (i.e., the secondary peak occurs at a significantly smaller bubble size), while the secondary peak becomes much broader and occurs at larger bubble sizes for larger values of the diffusivity.

The determination of the solid-bubble cutoff is based on Kr melting. Figure 5 shows the calculated bubble distribution at 500°C and at a fluence of 2×10^{20} m^{-2} using the values of the parameters listed in Table 1. Also shown in Fig. 10 is the Kr density in the bubbles calculated using Ronchi's modified hard-sphere equation of state for Kr (eqs. 14-17). The dotted horizontal line at a Kr density of 2.25×10^{28} atoms$\cdot m^{-3}$ is based on bulk Kr melting [17]. The cutoff radius used in the GRASS-SST calculations is determined as the radius at which the density of bulk Kr at melting (dotted line) is equal to the calculated Kr density within the bubbles. As can be seen from Fig. 5, this cutoff occurs at about 21 Å.

Figures 6 and 7 show the GRASS-SST calculated Kr size distributions, F_i, at 500°C as a function of Kr fluence using the values of the parameters shown in Table 1. Figures 6 and 7 are to be compared to the data shown in Fig. 2. As is evident, the theory predicts the trends in the evolution of the Kr size distribution with fluence shown in Fig. 2 and discussed in section 2: a distribution of solid Kr precipitates with fixed radii, and a distribution of larger gas or liquid filled bubbles which evolve to larger sizes for larger values of the Kr fluence. The predicted distribution of large bubbles at 4×10^{20} m^{-2} shown in Fig. 7 is broader than the observed distribution shown in

Fig. 2. The reason for this is that during the irradiation, the larger bubbles rupture to the specimen surface and vent their gas. This release mechanism has not been included in the calculations.

5. Discussion

The above analysis indicate that the value of the solid Kr bubble cutoff in Ni determines to a large degree the upper size limit of the small bubble peak in the Kr bubble-size distribution. However, one has yet to explain why the predicted cutoff based on the equation of state for Kr is smaller than the experimentally observed cutoff of about 30 Å (see Fig. 1). One explanation for this apparent discrepancy is that the use of the Kr equation of state ignores the Ni-Kr interactions at the bubble surface. For relatively small bubbles a large fraction of the Kr atoms have Ni nearest neighbors, and this should be included in the determination of the solid-bubble-size cutoff.

In order to assess this effect, an interactive Kr-Ni Lennard-Jones (12,7) potential has been generated based on a Lorentz-Berthelot mixture of species [18]. For a Lennard-Jones potential (eq. 10), the interactive ε is given by the geometric mean of the ε's from the Kr-Kr and the Ni-Ni potentials, and interactive σ is obtained from the arithmetic mean of the respective σ's. Table 2 gives the values of the ε's and σ's used for the interactive Kr-Ni potential.

Table 2.
Values of Lennard-Jones Parameters used for the Construction of an Interactive Kr-Ni Potential

	Kr	Ni	Kr-Ni
ε/k	211.3	348	271.2
σ	3.53	2.283	2.9065

Figure 8 shows the Kr size distribution calculated using the Kr-Ni parameters shown in Table 2. Also shown are the calculated Kr densities within bubbles using either the Kr-Ni interactive potential or the Kr equation of state. The dotted horizontal line in Fig. 8 is the density at which bulk Kr melts. This dotted line intersects the Kr density distribution calculated with the Kr equation of state at about a bubble radius of 21 Å (see Fig. 10). On the other hand, the dotted line intersects the Kr density curve made with the Kr-Ni interactive potential at a bubble radius of about 40 Å. One would expect that the physical cutoff would be somewhere in-between that obtained using the Kr-Kr potential and that obtained using the Kr-Ni potential. This analysis is consistent with the observed cutoff occurring at about 30 Å.

6. Conclusions

A rate theory for the evolution of the precipitate-size distribution of implanted noble gas ions in metals has been applied to the analysis of ion-implantation experiments. At temperatures of 400°C or higher, the implanted precipitates evolve into a bi-modal size distribution containing small solid precipitates and an additional population of larger, faceted bubbles. The analysis indicates that the solid precipitates are immobile while the larger bubbles move by surface diffusion control during the implantation process. The maximum radius at which the precipitates are solid (solid cutoff) determines the location of the peak of the solid-precipitate size distribution. The magnitude of the bubble mobility determines the location of the peak of the size distribution of the gas or liquid filled bubbles.

Analyses performed using a solid cutoff determined by the intersection of the bulk solid-gas density with the gas density within bubbles distribution,

determined using an equation of state based on a perturbed hard-sphere model, are in agreement with the observed trends for the behavior of the precipitate size distribution as a function of temperature and ion fluence.

The calculated solid cutoff is smaller than that which is observed. The reason for this discrepancy is attributed to the use of a noble gas equation of state which ignores the metal-gas interactions at the bubble surface.

References

1. R. C. Birtcher and A. S. Liu, "Temperature Dependence of Kr Precipitation in Ni",
2. D. Preinninger and D. Kaletta, J. Nucl. Mater., 117 (1983) 239-243.
3. L. K. Mansur and W. A. Coghlan, J. Nucl. Mater. 119 (1983) 1.
4. E. Ya Mikhlin, J. Nucl. Mater. 87 (1979) 405.
5. W. Nixon and D. A. Macinnes, J. Nucl. Mater. 101 (1981) 192-199.
6. N. Marochov, L. J. Perryman and P. J. Goodhew, J. Nucl. Mater. 149 (1987) 296-301.
7. J. Biersack and L. G. Haggmark, Nucl. Instr. and Meth. 174, (1980) 257.
8 H. H. Andersen and H. L. Bay, in Sputtering by Particle Bombardment, I. R. Behrisch, ed., Topic Appl. Phys., Vol. 47 (Springer, Berlin 1981), p. 145.
9. J. Rest, "GRASS-SST" A Comprehensive, Mechanistic Model for the Prediction of Fission-gas Behavior in UO_2-base Fuels during Steady-state and Transient Conditions", NUREG/CR-0202, Argonne National Laboratory Report ANL-78-53 (1978).
10. J. Rest and A. W. Cronenberg, J. Nucl. Mater. 150 (1987) 203-225.
11. L. E. Willertz and P. G. Shewmon, Met. Trans. 1 (1970) 2217.
12. W. Beere, J. Nucl. Mater. 45 (1972/73) 91.
13. F. A. Nichols and C. Ronchi, Adv. Cerm. 17 (1986) 85.
14. E. E. Gruber, J. Appl. Phys. 38 (1967) 243-250.
15. E. E. Gruber, ANL-78-36 (April 1978).
16. C. Ronchi, J. Nucl. Mater. 96 (1981) 314-328.
17. P. H. Lahr and G. Eversole, Jour. Chem. and Eng. Data, 7 (1962) 42.
18. J. S. Rowlinson and F. L. Swinton, "Liquids and Liquid Mixtures", Butterworths Monographs in Chemistry, Butterworth Scientific (1982).

Figure Captions

Fig. 1. TEM micrographs for Ni implanted at 500°C with 0.7 (left side) and 2.0 (right side) x 10^{20} Kr^{+} m^{-2}.

Fig. 2. Measured Kr bubble density in Ni as a function of bubble radius for different Kr fluences.

Fig. 3. Calculated Kr bubble-size distribution for three valves of the solid-bubbles cutoff.

Fig. 4. Calculated Kr bubble-size distribution for three valves of the gas-bubbles diffusivity.

Fig. 5. Calculated Kr density within bubbles compared to the density at which solid Kr melts (dotted line).

Fig. 6. Calculated Kr bubble-size distribution as a function of Kr fluence.

Fig. 7. Calculated Kr bubble-size distribution as a function of Kr fluence.

Fig. 8. Calculated Kr density within bubbles using Kr-Kr potential or Kr-Ni potential (Table 2) compared to the density at which solid Kr melts (dotted line).

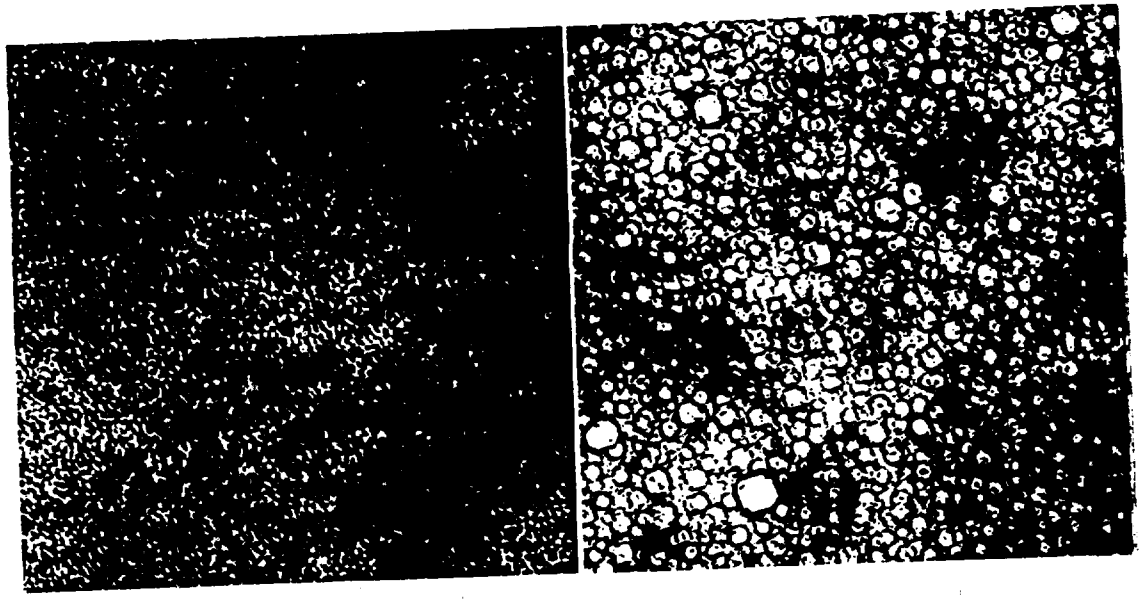

Fig. 1

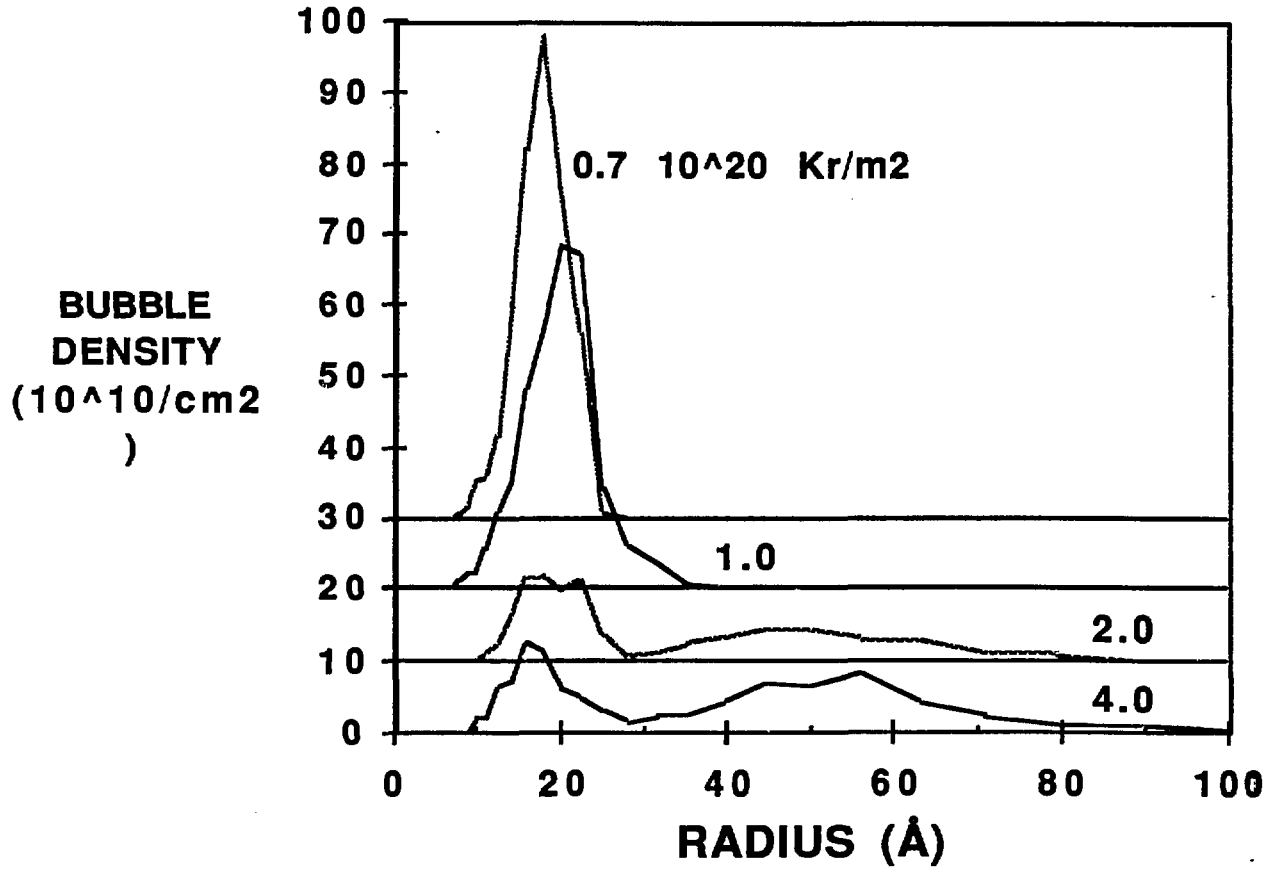
BUBBLE DENSITY (10^10/cm2)
100
90
80
70
60
50
40
30
20
10
0
0.7 10^20 Kr/m2
1.0
2.0
4.0
0
20
40
60
80
100
RADIUS (Å)

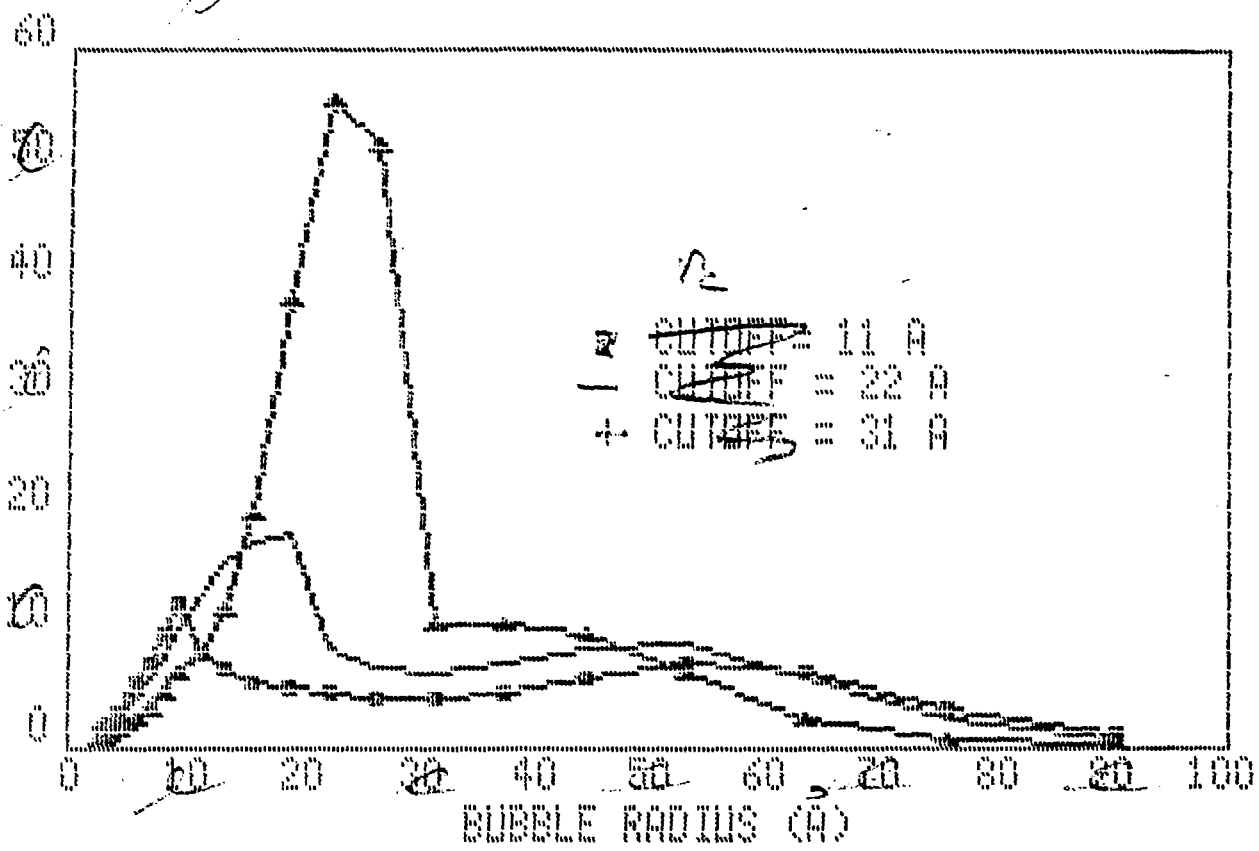
Kr in NL at 500 C, 2x10^16 n/cm^2 THERM
BUBBLE DISTRIBUTION VS SOLID Kr CUTOFF
BUBBLE DENSITY (10^23 m^-3)
0
20
40
60
0
10
20
30
40
50
60
70
80
90
100
BUBBLE RADIUS (A)
CUTOFF = 11 A
CUTOFF = 22 A
CUTOFF = 31 A

Fig. 3

Fig. 4 Kr in Ni at 500 C; 2×10^16 THEORY

BUBBLE DISTRIBUTION vs Db

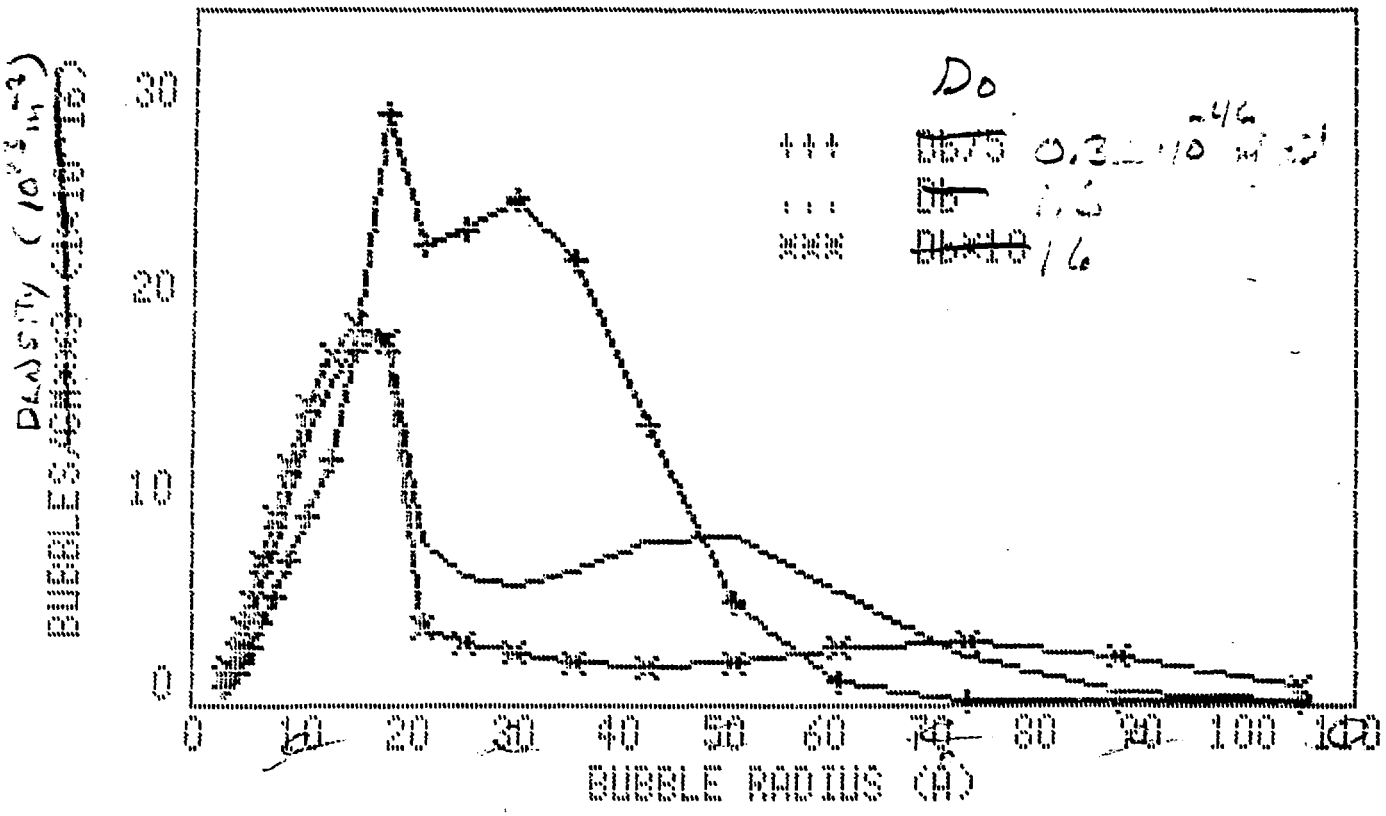

effect of D_0^B

Fig. 4

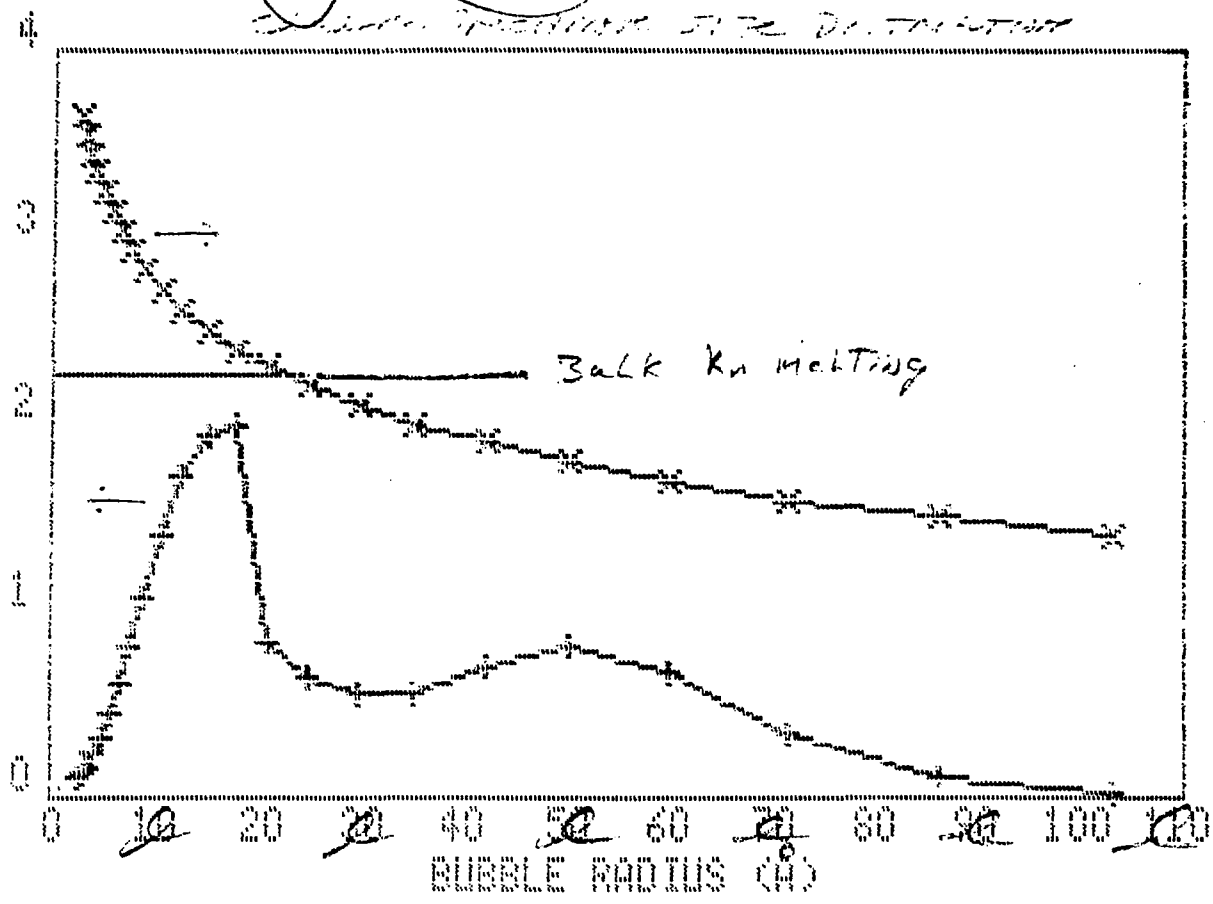

FIG. 5

Kr in Ni at 500 °C

BUBBLE DISTRIBUTION vs FLUENCE

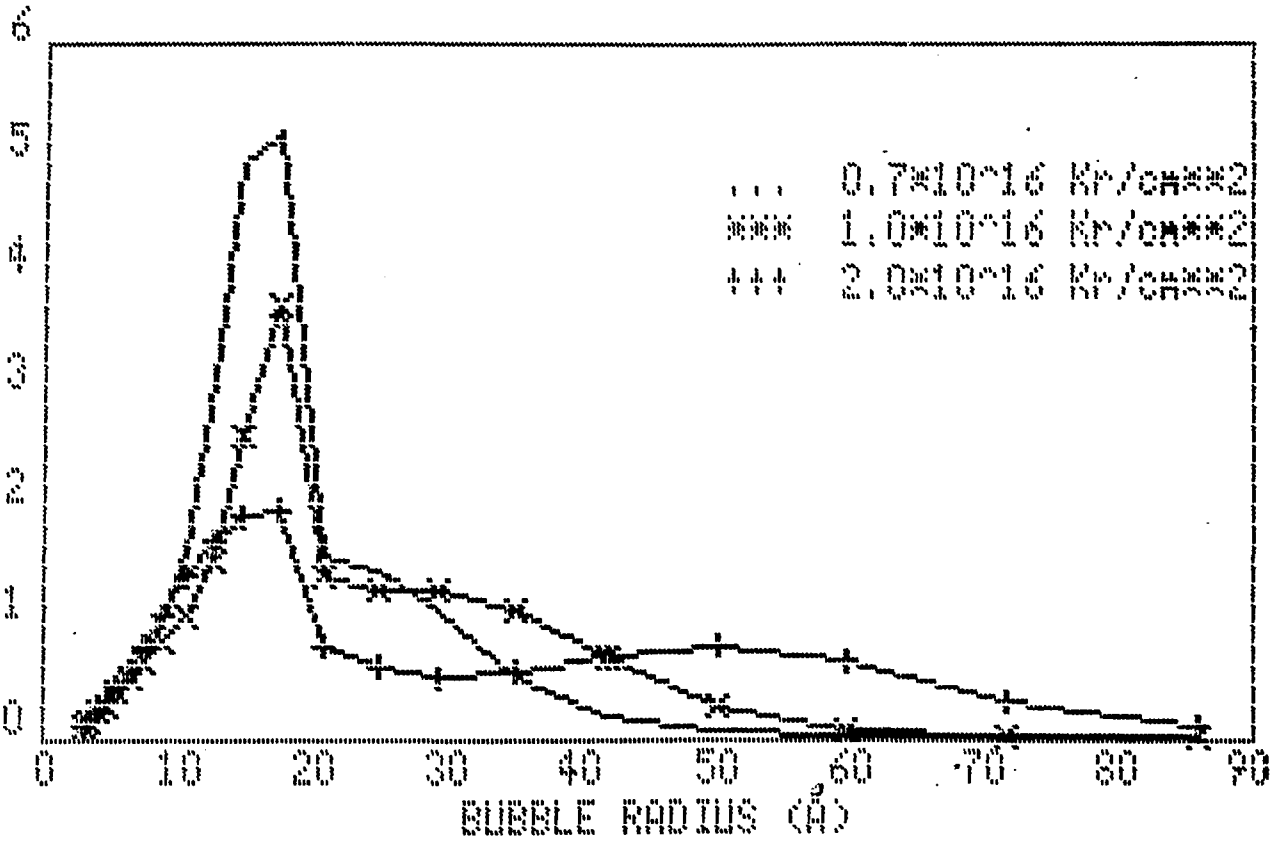

Fig. 6

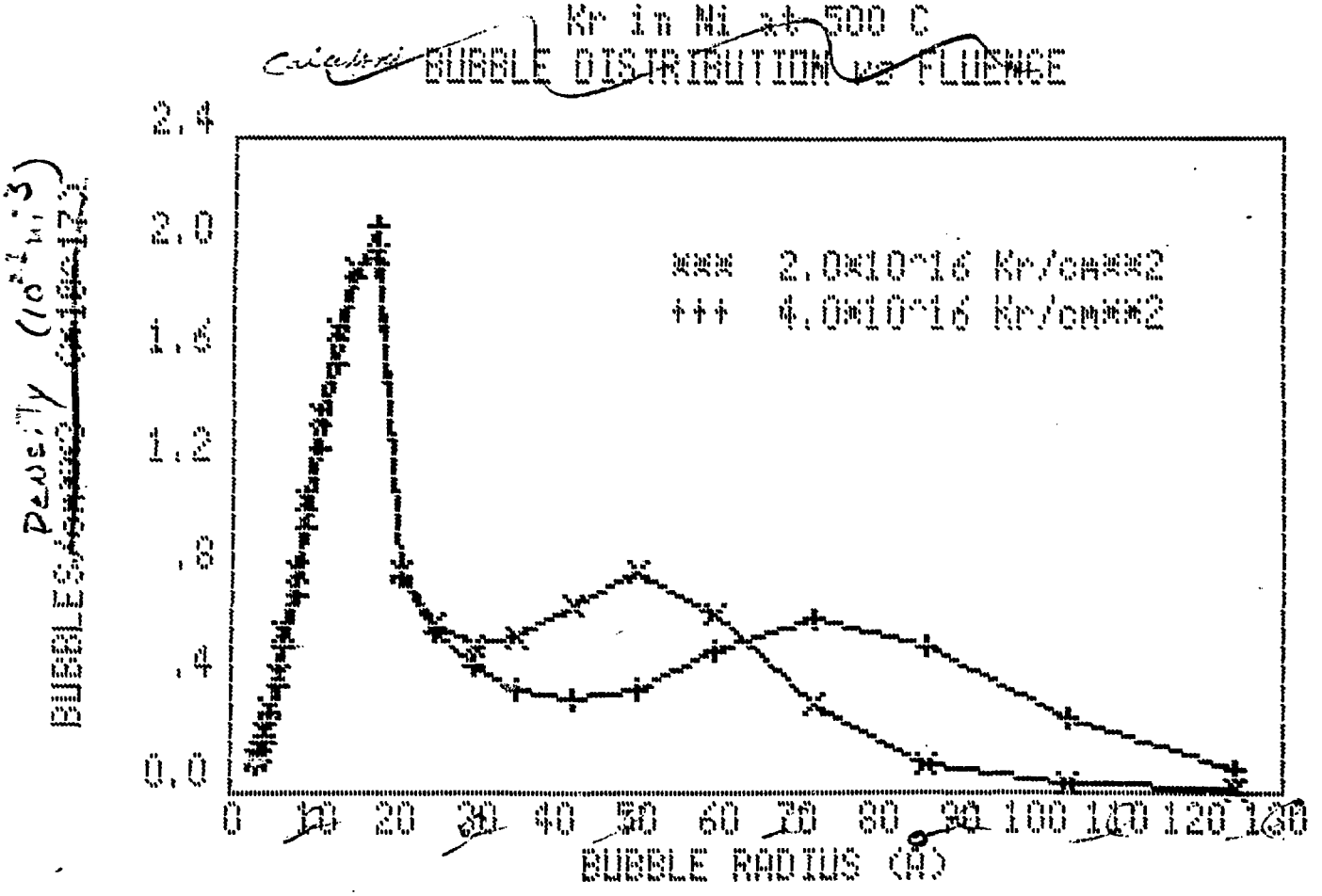
Kr in Ni at 500 C
BUBBLE DISTRIBUTION vs FLUENCE
BUBBLES/cm**3 (10**18)
2.4
2.0
1.6
1.2
0.8
0.4
0.0
*** 2.0*10^16 Kr/cm**2
+++ 4.0*10^16 Kr/cm**2
0
10
20
30
40
50
60
70
80
90
100
110
120
130
BUBBLE RADIUS (A)

Fig. 7

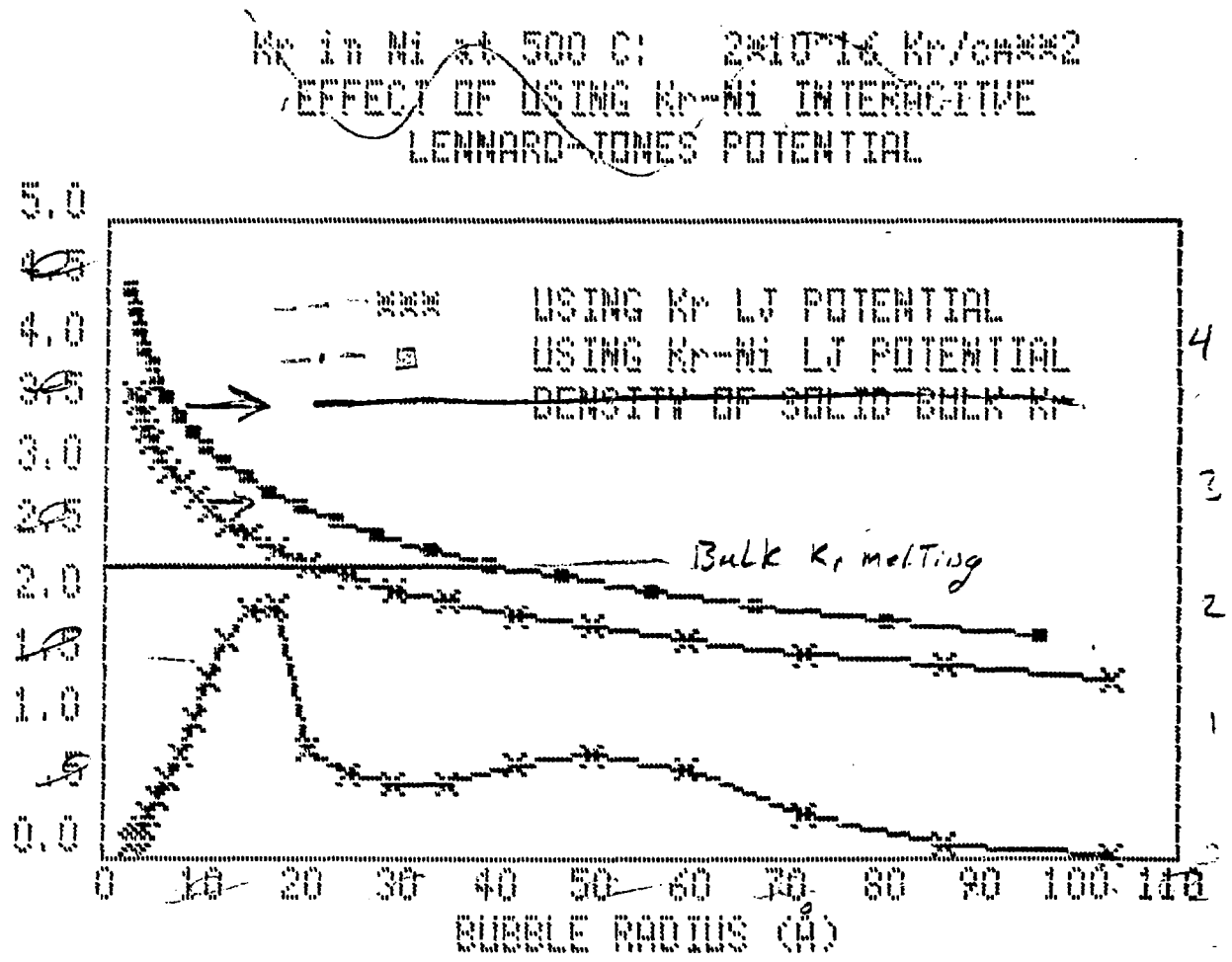
Kr in Ni @ 500 C: 2x10^14 Kr/cm**2
EFFECT OF USING Kr-Ni INTERACTIVE LENNARD-JONES POTENTIAL
USING Kr LJ POTENTIAL
USING Kr-Ni LJ POTENTIAL
DENSITY OF SOLID BULK Kr
Bulk Kr melting
BUBBLE DENSITY (10^23 m^-3)
BUBBLE RADIUS (Å)
0.0
0.5
1.0
1.5
2.0
2.5
3.0
3.5
4.0
4.5
5.0
0
10
20
30
40
50
60
70
80
90
100
110
1
2
3
4

8

FS 14